

# Supplementary material

## Nearly constant Q dissipative models and wave equations for general viscoelastic anisotropy

Qi Hao<sup>a,\*</sup>, Stewart Greenhalgh<sup>b</sup>

<sup>a</sup>*CPG, KFUPM, Dhahran, 31261, Saudi Arabia*

<sup>b</sup>*Institute of Geophysics, ETH Zurich, Zurich, 8092, Switzerland*

### Abstract

This document provides the supplementary material for the RSPA journal article “Hao, Q., and S. Greenhalgh, 2021, Nearly constant Q dissipative models and wave equations for general viscoelastic anisotropy”, the doi of which is 10.1098/rspa.2021.0170. This journal article is abbreviated as HG2021 throughout this document for brevity. In this document, we show: (1) the quality factor and phase velocity of a plane wave in a viscoelastic orthorhombic medium; (2) the complex stiffness coefficients for our nearly constant  $Q$  models and the Kolsky and Kjartansson models in the orthorhombic case; (3) the Thomsen parameters for orthorhombic anisotropy; (4) numerical comparisons for the quality factors, phase velocities and Thomsen parameters from our models and the Kolsky and Kjartansson models; (5) the derivation of the viscoelastic isotropic wave equations for our nearly constant  $Q$  wave equations; (6) a numerical example of implementing the viscoelastic isotropic wave equations for our nearly constant  $Q$  models in wave propagation modeling.

*Keywords:* seismic, viscoelastic, isotropic, anisotropic, Q

### 1. Plane-wave quality factor and phase velocity for a viscoelastic orthorhombic medium

Referring to [1], the complex velocities for homogeneous plane waves in a viscoelastic orthorhombic medium are determined by the eigenvalues of the Christoffel matrix for orthorhombic anisotropy, namely

$$\det \begin{pmatrix} \Gamma_{11} - \rho v^2 & \Gamma_{12} & \Gamma_{13} \\ \Gamma_{12} & \Gamma_{22} - \rho v^2 & \Gamma_{23} \\ \Gamma_{13} & \Gamma_{23} & \Gamma_{33} - \rho v^2 \end{pmatrix} = 0, \quad (1)$$

with

$$\Gamma_{11} = M_{11}n_1^2 + M_{66}n_2^2 + M_{55}n_3^2, \quad (2)$$

$$\Gamma_{22} = M_{66}n_1^2 + M_{22}n_2^2 + M_{44}n_3^2, \quad (3)$$

$$\Gamma_{33} = M_{55}n_1^2 + M_{44}n_2^2 + M_{33}n_3^2, \quad (4)$$

$$\Gamma_{12} = (M_{12} + M_{66})n_1n_2, \quad (5)$$

$$\Gamma_{13} = (M_{13} + M_{55})n_1n_3, \quad (6)$$

$$\Gamma_{23} = (M_{23} + M_{44})n_2n_3. \quad (7)$$

Here,  $\rho$  denotes density. Quantities  $M_{ij}$  denote the complex stiffness coefficients. Vector  $(n_1, n_2, n_3)^T$  denotes the plane-wave propagation direction. Quantity  $v$  denotes the complex velocity. For a given propagation direction,

\*Corresponding author

Email addresses: xqi.hao@gmail.com, qi.hao@kfupm.edu.sa (Qi Hao), gstewart@retired.ethz.ch (Stewart Greenhalgh)

equation 1 gives rise to the complex velocities for three waves, viz the quasi-compressional waves and the two quasi-shear waves. Sorting the real part of the complex velocities for a given propagation direction, we make a convention that the real part of the S<sub>1</sub>-wave complex velocity is no less than that of the S<sub>2</sub>-wave complex velocity, namely  $\text{Re}(v_{S1}) \geq \text{Re}(v_{S2})$ .

Referring to [2] and [3], the quality factor ( $Q$ ) and phase velocity  $V$  for a homogeneous plane wave are given by

$$Q = -\frac{\text{Re}(v^2)}{\text{Im}(v^2)}, \quad V = \frac{v_R^2 + v_I^2}{v_R}. \quad (8)$$

Here,  $v = v_R - i\text{sgn}(\omega)v_I$  denotes the complex velocity, the square of which is an eigenvalue of the Christoffel matrix [1]. The minus sign corresponds to the Fourier transform definition in HG2021. Quantities  $v_R$  and  $v_I$  are real valued. The above definitions for  $Q$  and  $V$  were given by [2] and [3], respectively.

## 2. Nearly constant $Q$ dissipative models for orthorhombic anisotropy

We show the Kolsky and Kjartansson models and our proposed dissipative models in the orthorhombic case below.

The complex stiffness matrix for the Kjartansson model is given by

$$\mathbf{M} = \begin{pmatrix} M_{11}^{(0)}\Lambda_{11} & M_{12}^{(0)}\Lambda_{12} & M_{13}^{(0)}\Lambda_{13} & 0 & 0 & 0 \\ M_{12}^{(0)}\Lambda_{12} & M_{22}^{(0)}\Lambda_{22} & M_{23}^{(0)}\Lambda_{23} & 0 & 0 & 0 \\ M_{13}^{(0)}\Lambda_{13} & M_{23}^{(0)}\Lambda_{23} & M_{33}^{(0)}\Lambda_{33} & 0 & 0 & 0 \\ 0 & 0 & 0 & M_{44}^{(0)}\Lambda_{44} & 0 & 0 \\ 0 & 0 & 0 & 0 & M_{55}^{(0)}\Lambda_{55} & 0 \\ 0 & 0 & 0 & 0 & 0 & M_{66}^{(0)}\Lambda_{66} \end{pmatrix}, \quad (9)$$

where  $\Lambda_{ij}$  are given by

$$\Lambda_{ij} = \left(-i\frac{\omega}{\omega_0}\right)^{2\gamma_{ij}} \quad (10)$$

with

$$\gamma_{ij} = \frac{1}{\pi} \arctan \left( \frac{1}{Q_{ij}} \right). \quad (11)$$

The complex stiffness matrix for the Kolsky model is given by

$$\mathbf{M}(\omega) = \mathbf{M}^{(0)} + \mathbf{M}^{(1)} \left[ \frac{2}{\pi} \ln \left| \frac{\omega}{\omega_0} \right| - i\text{sgn}(\omega) \right]. \quad (12)$$

The complex stiffness matrix for the first-order nearly constant  $Q$  model is expressed as

$$\mathbf{M}(\omega) = \mathbf{M}^{(0)} + \mathbf{M}^{(1)} [W(\omega) - W_R(\omega_0)], \quad (13)$$

where  $W(\omega)$  denotes the weighting function and  $W_R(\omega_0)$  denotes the real part of the weighting function at the reference angular frequency  $\omega_0$ . The weighting function is given by

$$W(\omega) = \sum_{\ell=1}^L \frac{1 - i\omega\tau_{\epsilon}^{(\ell)}}{1 - i\omega\tau_{\sigma}^{(\ell)}}, \quad (14)$$

where  $L$  denotes the total number of SLS elements. The minus sign in front of “ $i$ ” corresponds to the sign convention in the exponential term of the Fourier transform (equations 1.1 and 1.2 of HG2021). Quantities  $\tau_\epsilon^{(\ell)}$  and  $\tau_\sigma^{(\ell)}$  are  $Q$ -independent strain and stress relaxation times in the  $l$ -th term (SLS element) in the summation for the weighting function, respectively.

The complex stiffness matrix for the second-order nearly constant  $Q$  model is given by

$$\mathbf{M}(\omega) = \mathbf{M}^{(0)} + \mathbf{M}^{(1)} [W(\omega) - W_R(\omega_0)] + \frac{1}{2} \mathbf{M}^{(2)} [W(\omega) - W_R(\omega_0)]^2. \quad (15)$$

For orthorhombic anisotropy,  $\mathbf{M}^{(n)}$ ,  $n = 0, 1, 2$ , in equations 12, 13 and 15 are given by

$$\mathbf{M}^{(n)} = \begin{pmatrix} \frac{M_{11}^{(0)}}{Q_{11}^n} & \frac{M_{12}^{(0)}}{Q_{12}^n} & \frac{M_{13}^{(0)}}{Q_{13}^n} & 0 & 0 & 0 \\ \frac{M_{12}^{(0)}}{Q_{12}^n} & \frac{M_{22}^{(0)}}{Q_{22}^n} & \frac{M_{23}^{(0)}}{Q_{23}^n} & 0 & 0 & 0 \\ \frac{M_{13}^{(0)}}{Q_{13}^n} & \frac{M_{23}^{(0)}}{Q_{23}^n} & \frac{M_{33}^{(0)}}{Q_{33}^n} & 0 & 0 & 0 \\ 0 & 0 & 0 & \frac{M_{44}^{(0)}}{Q_{44}^n} & 0 & 0 \\ 0 & 0 & 0 & 0 & \frac{M_{55}^{(0)}}{Q_{55}^n} & 0 \\ 0 & 0 & 0 & 0 & 0 & \frac{M_{66}^{(0)}}{Q_{66}^n} \end{pmatrix}, \quad (16)$$

where  $Q_{ij}^n$  at  $n = 0$  is assigned as one even for  $Q_{ij} = \infty$ .

### 3. Thomsen anisotropy parameters

For a viscoelastic anisotropic medium, the non-zero independent complex stiffness coefficients are generally expressed as

$$M_{ij} = M_{ij}^R \left( 1 - i \operatorname{sgn}(\omega) \frac{1}{\tilde{Q}_{ij}} \right), \quad (17)$$

where  $M_{ij}^R$  and  $\tilde{Q}_{ij}$  are even functions of frequency. For orthorhombic anisotropy, the symmetry pattern of matrix  $\mathbf{M}$  is similar to that of equation 16.

Table 1: A summary of the Thomsen parameters for velocity and attenuation anisotropies. The indices “1”, “2” and “3” denote the  $x$ ,  $y$  and  $z$  axes normals to the planes in which the Thomsen parameters are defined.

|                        | [ $y, z$ ] plane                          | [ $x, z$ ] plane                          | [ $x, y$ ] plane |
|------------------------|---|---|------------------|
| velocity anisotropy    | $\epsilon_1, \delta_1, \gamma_1$          | $\epsilon_2, \delta_2, \gamma_2$          | $\delta_3$       |
| attenuation anisotropy | $\epsilon_{Q1}, \delta_{Q1}, \gamma_{Q1}$ | $\epsilon_{Q2}, \delta_{Q2}, \gamma_{Q2}$ | $\delta_{Q3}$    |

Referring to [4] and [5], Table 1 summarizes the Thomsen anisotropy parameters for velocity and attenuation. The parameters  $\epsilon_1$  and  $\delta_1$  describe the anisotropy of the velocities of P-waves and in-plane S-waves in the [ $y, z$ ] plane. The parameter  $\gamma_1$  describes the anisotropy of the velocities of the anti-plane S-waves in the [ $y, z$ ] plane. Here, the terminology “anti-plane” means being polarized in the direction perpendicular to the plane of interest. The parameters  $\epsilon_2$  and  $\delta_2$  describe the anisotropy of the velocities of P-waves and in-plane S-waves in the [ $x, z$ ] plane. The parameter  $\gamma_2$  describes the anisotropy of the velocities of the anti-plane S-waves in the [ $x, z$ ] plane. The parameter  $\delta_3$  describes the anisotropy of the velocities of the in-plane P-waves in the [ $x, y$ ] plane with the  $x$  axis viewed as the symmetry axis. The parameters  $\epsilon_{Q1}$  and  $\delta_{Q1}$  describe the anisotropy of the wavenumber-normalized attenuation coefficients (WNACs) of P-waves and in-plane S-waves in the [ $y, z$ ] plane. The parameter  $\gamma_{Q1}$  describes the anisotropy of the WNACs of the anti-plane S-waves in the [ $y, z$ ] plane. The parameters  $\epsilon_{Q2}$  and  $\delta_{Q2}$  describe

the anisotropy of WNACs of P-waves and in-plane S-waves in the  $[x, z]$  plane. The parameter  $\gamma_{Q1}$  describes the anisotropy of the WNACs of the anti-plane S-waves in the  $[x, z]$  plane. The parameter  $\delta_{Q3}$  describes the anisotropy of the WNACs of the in-plane P-waves in the  $[x, y]$  plane with the  $x$  axis viewed as the symmetry axis. All these parameters are defined below.

- $\epsilon_1, \delta_1, \gamma_1$ : the Thomsen parameters defined in the  $[y, z]$  symmetry plane (the subscript 1 corresponds to the  $x$ -axis normal to the  $[y, z]$  plane)

$$\epsilon_1 \equiv \frac{M_{22}^R - M_{33}^R}{2M_{33}^R}, \quad (18)$$

$$\delta_1 \equiv \frac{(M_{23}^R + M_{44}^R)^2 - (M_{33}^R - M_{44}^R)^2}{2M_{33}^R(M_{33}^R - M_{44}^R)}, \quad (19)$$

$$\gamma_1 \equiv \frac{M_{66}^R - M_{55}^R}{2M_{55}^R}. \quad (20)$$

- $\epsilon_2, \delta_2, \gamma_2$ : the Thomsen parameters defined in the  $[x, z]$  symmetry plane (the subscript 2 corresponds to the  $y$ -axis normal to the  $[x, z]$  plane)

$$\epsilon_2 \equiv \frac{M_{11}^R - c_{33}^R}{2c_{33}^R}, \quad (21)$$

$$\delta_2 \equiv \frac{(M_{13}^R + M_{55}^R)^2 - (M_{33}^R - M_{55}^R)^2}{2M_{33}^R(M_{33}^R - M_{55}^R)}, \quad (22)$$

$$\gamma_2 \equiv \frac{M_{66}^R - M_{44}^R}{2M_{44}^R}. \quad (23)$$

- $\delta_3$ : the Thomsen parameter defined in the  $[x, y]$  symmetry plane (the subscript 3 corresponds to the  $z$ -axis normal to the  $[x, y]$  plane and the  $x$ -axis plays the role of the symmetry axis)

$$\delta_3 \equiv \frac{(M_{12}^R + M_{66}^R)^2 - (M_{11}^R - M_{66}^R)^2}{2M_{11}^R(M_{11}^R - M_{66}^R)}. \quad (24)$$

- $\epsilon_{Q1}, \delta_{Q1}, \gamma_{Q1}$ : the Thomsen parameters for attenuation anisotropy defined in the  $[y, z]$  symmetry plane

$$\epsilon_{Q1} \equiv \frac{\tilde{Q}_{33} - \tilde{Q}_{22}}{\tilde{Q}_{22}}, \quad (25)$$

$$\delta_{Q1} \equiv \frac{\frac{\tilde{Q}_{33} - \tilde{Q}_{44}}{\tilde{Q}_{44}} M_{44}^R \frac{(M_{23}^R + M_{33}^R)^2}{M_{33}^R - M_{44}^R} + 2 \frac{\tilde{Q}_{33} - \tilde{Q}_{23}}{\tilde{Q}_{23}} M_{23}^R (M_{23}^R + M_{44}^R)}{M_{33}^R (M_{33}^R - M_{44}^R)}, \quad (26)$$

$$\gamma_{Q1} \equiv \frac{\tilde{Q}_{55} - \tilde{Q}_{66}}{\tilde{Q}_{66}} \quad (27)$$

- $\epsilon_{Q2}, \delta_{Q2}, \gamma_{Q2}$ : the Thomsen parameters for attenuation anisotropy defined in the  $[x, z]$  symmetry plane

$$\epsilon_{Q2} \equiv \frac{\tilde{Q}_{33} - \tilde{Q}_{11}}{\tilde{Q}_{11}}, \quad (28)$$

$$\delta_{Q2} \equiv \frac{\frac{\tilde{Q}_{33} - \tilde{Q}_{55}}{\tilde{Q}_{55}} M_{55}^R \frac{(M_{13}^R + M_{33}^R)^2}{M_{33}^R - M_{55}^R} + 2 \frac{\tilde{Q}_{33} - \tilde{Q}_{13}}{\tilde{Q}_{13}} M_{13}^R (M_{13}^R + M_{55}^R)}{M_{33}^R (M_{33}^R - M_{55}^R)}, \quad (29)$$

$$\gamma_{Q2} \equiv \frac{\tilde{Q}_{44} - \tilde{Q}_{66}}{\tilde{Q}_{66}}. \quad (30)$$

- $\delta_{Q3}$ : the Thomsen parameter for attenuation anisotropy defined in the  $[x, y]$  symmetry plane

$$\delta_{Q3} \equiv \frac{\tilde{Q}_{11}-\tilde{Q}_{66} M_{66}^R \frac{(M_{11}^R+M_{12}^R)^2}{M_{11}^R-M_{66}^R} + 2 \tilde{Q}_{11}-\tilde{Q}_{12} M_{12}^R (M_{12}^R + M_{66}^R)}{M_{11}^R (M_{11}^R - M_{66}^R)}. \quad (31)$$

#### 4. Numerical comparisons between our models with the Kolsky and Kjartansson models

We follow the model parameters shown in equations 3.43 of HG2021. The medium density is set as  $\rho = 10^3 \text{ kg/m}^3$ . The reference stiffness coefficients and quality factors are designed as

$$\mathbf{M}^{(0)} = \begin{pmatrix} 9.00 & 3.60 & 2.25 & 0 & 0 & 0 \\ & 9.84 & 2.40 & 0 & 0 & 0 \\ & & 5.94 & 0 & 0 & 0 \\ & & & 2.00 & 0 & 0 \\ & & & & 1.60 & 0 \\ & & & & & 2.18 \end{pmatrix}, \mathbf{Q} = \begin{pmatrix} 70 & 35 & 45 & \infty & \infty & \infty \\ & 60 & 48 & \infty & \infty & \infty \\ & & 50 & \infty & \infty & \infty \\ & & & 35 & \infty & \infty \\ & & & & 30 & \infty \\ & & & & & 40 \end{pmatrix}, \quad (32)$$

where  $\mathbf{M}^{(0)}$  and  $\mathbf{Q}$  are symmetric matrices and only their upper diagonal elements are shown for brevity. The units of  $\mathbf{M}^{(0)}$  are  $10^9 \text{ Pa}$ . Using the model parameters shown above, we initiate the complex stiffness coefficients 9, 12, 13 and 15 for the Kjartansson and Kolsky models and the first- and second-order models, respectively. For a given propagation direction, three complex velocities are obtained by solving equation 1. We show the variations of the quality factor, phase velocity and Thomsen parameters with frequency below.

##### 4.1. The variation of the quality factor with frequency

As a supplement to Figures 1 through 3 of HG2021, we take account of more propagation directions. Figures 1 through 9 show that the quality factors from the first- and second-order nearly constant  $Q$  models fit well with those from the Kolsky and Kjartansson models, respectively. Besides, these figures suggest that the Kjartansson model is not exactly constant  $Q$  in the orthorhombic case.

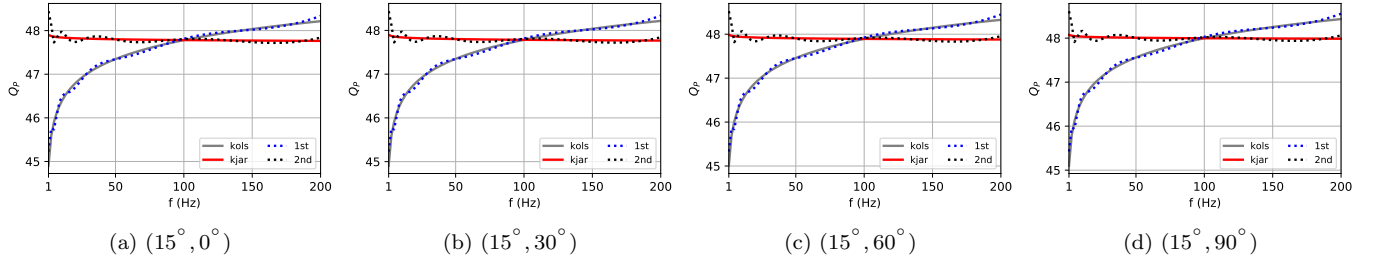


Figure 1: The quality factors of homogeneous plane P waves in dissipative models for orthorhombic anisotropy. Legend abbreviations “Kols”, “Kjar”, “1st” and “2nd” denote the Kolsky and Kjartansson models and the first- and second-order nearly constant  $Q$  models, respectively. The quantity  $(\theta, \phi)$  describes the wave propagation direction, where  $\theta$  denotes the polar angle measured from the  $z$  axis, and  $\phi$  denotes the azimuthal angle measured in the  $[x, y]$  plane and counterclockwise from the  $x$  axis. For example,  $(15^\circ, 0^\circ)$  denotes  $\theta = 15^\circ$  and  $\phi = 0^\circ$ .

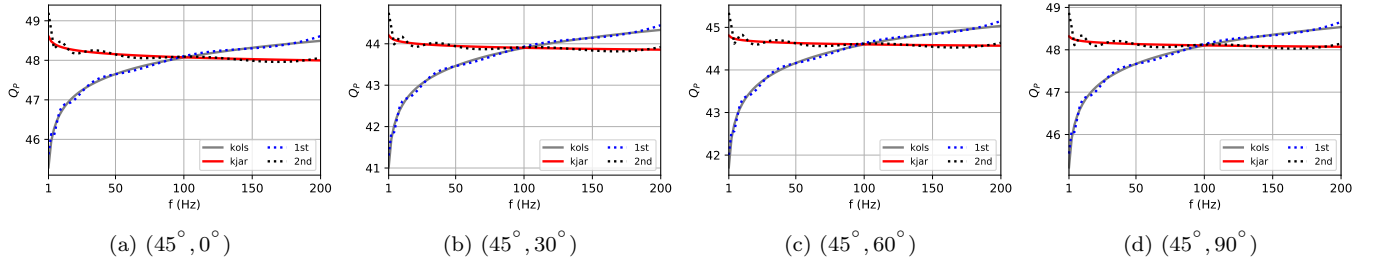


Figure 2: Similar to Figure 1 but for the P-waves with  $\theta = 45^\circ$ .

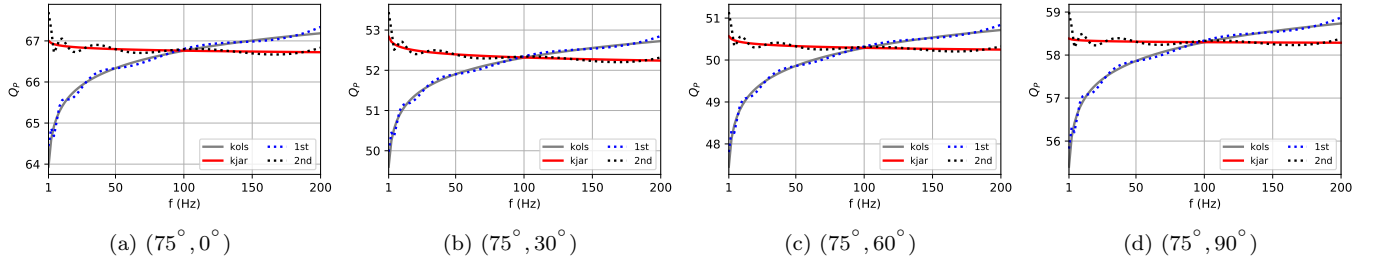


Figure 3: Similar to Figure 1 but for the P-waves with  $\theta = 75^\circ$ .

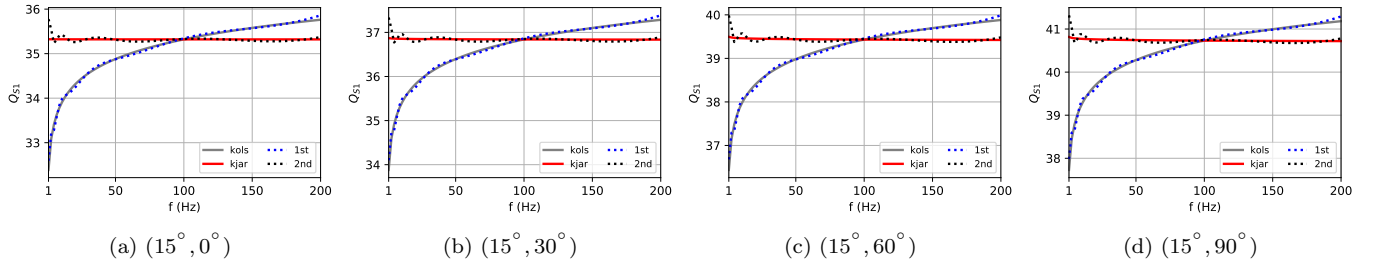


Figure 4: Similar to Figure 1 but for the S<sub>1</sub> waves with  $\theta = 15^\circ$ .

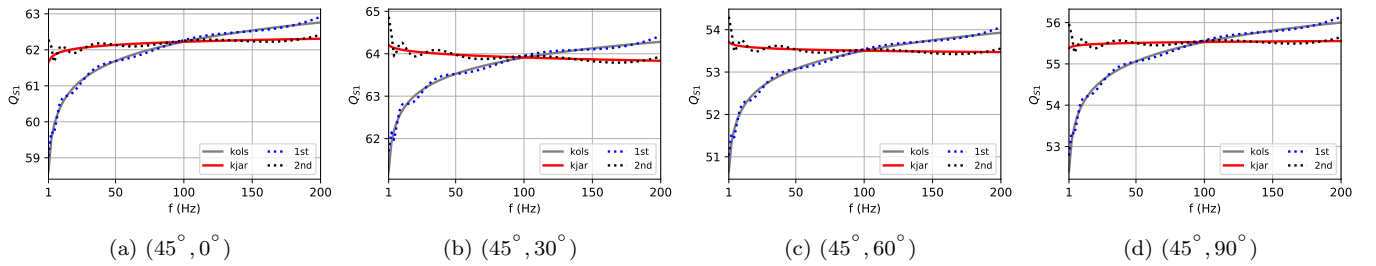


Figure 5: Similar to Figure 1 but for the S<sub>1</sub> waves with  $\theta = 45^\circ$ .

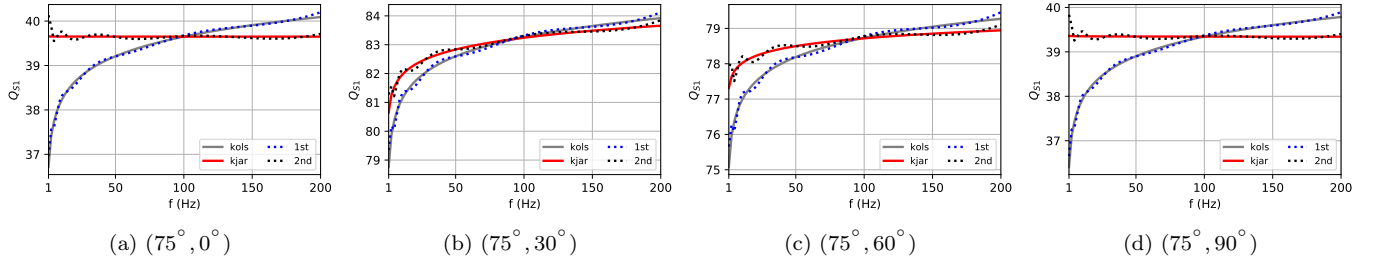


Figure 6: Similar to Figure 1 but for the  $S_1$  waves with  $\theta = 75^\circ$ .

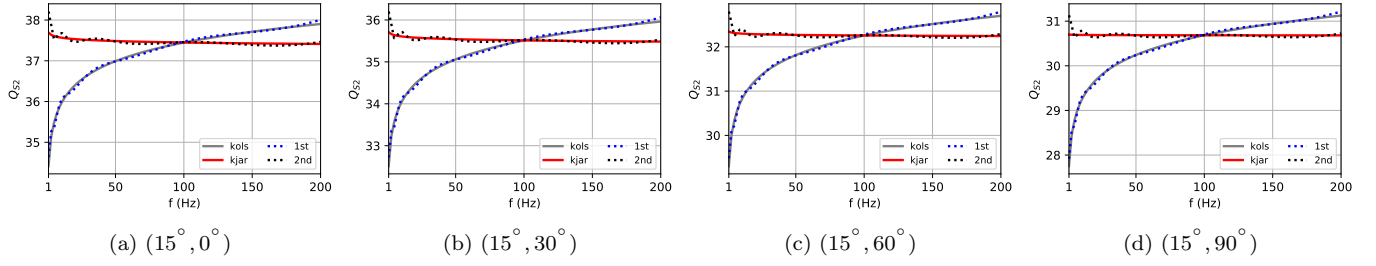


Figure 7: Similar to Figure 1 but for the  $S_2$  waves with  $\theta = 15^\circ$ .

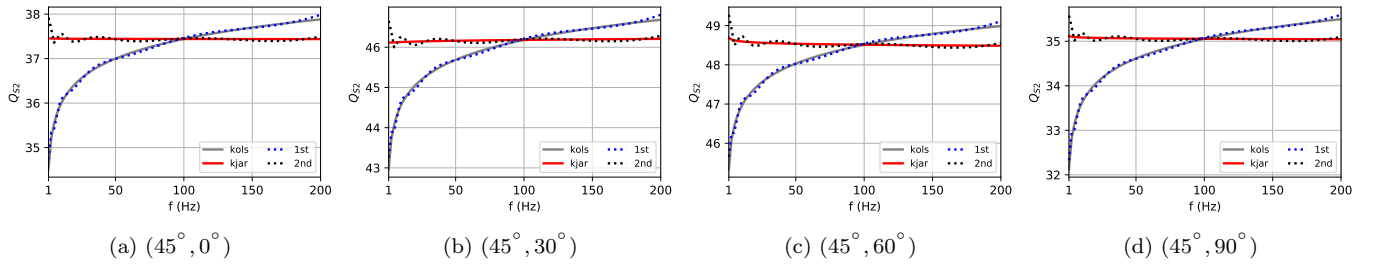


Figure 8: Similar to Figure 1 but for the  $S_2$  waves with  $\theta = 45^\circ$ .

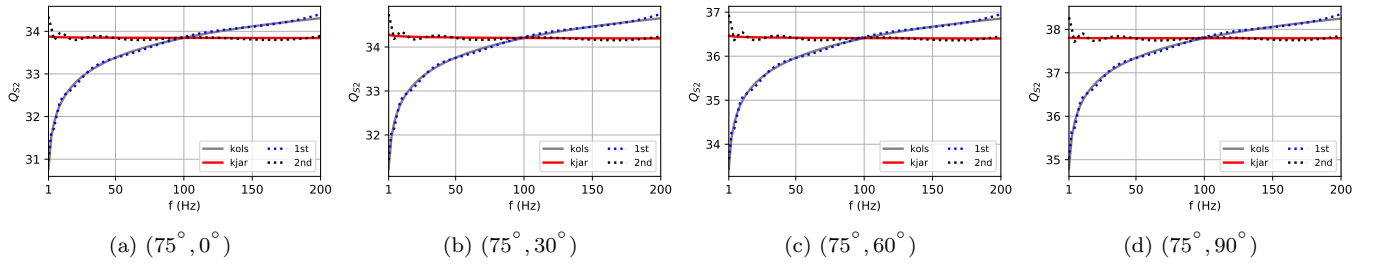


Figure 9: Similar to Figure 1 but for the  $S_2$  waves with  $\theta = 75^\circ$ .

#### 4.2. The variation of the phase velocity with frequency

As a supplement to Figures 4 through 6 of HG2021, we compute the phase velocities for a few propagation directions. As illustrated in Figures 10 through 18, the phase velocities from the first- and second-order nearly constant  $Q$  models are quite close to those from the Kolsky and Kjartansson models.

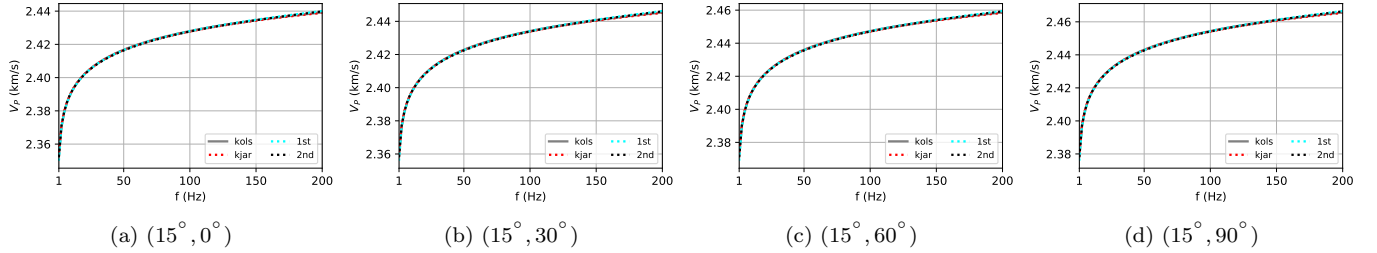


Figure 10: The phase velocities of homogeneous plane P waves in dissipative models for orthorhombic anisotropy. The abbreviations and the quantity  $(\theta, \phi)$  are explained in Figure 1.

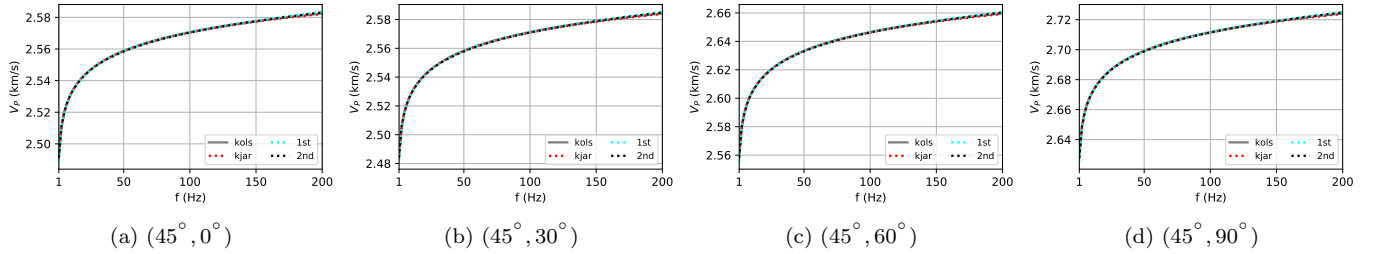


Figure 11: Similar to Figure 10 but for the P waves with  $\theta = 45^\circ$ .

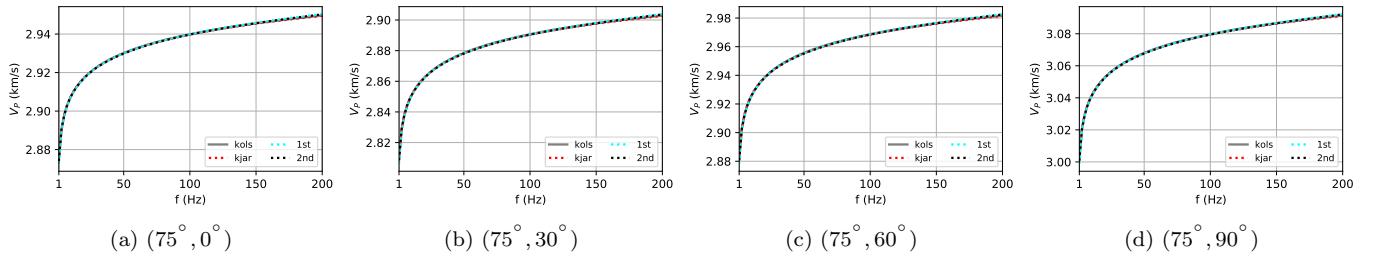


Figure 12: Similar to Figure 10 but for the P waves with  $\theta = 75^\circ$ .

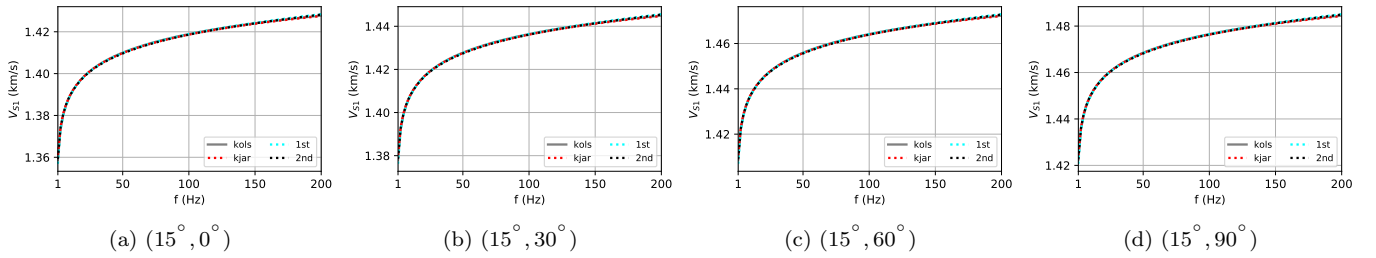


Figure 13: Similar to Figure 10 but for the  $S_1$  waves with  $\theta = 15^\circ$ .

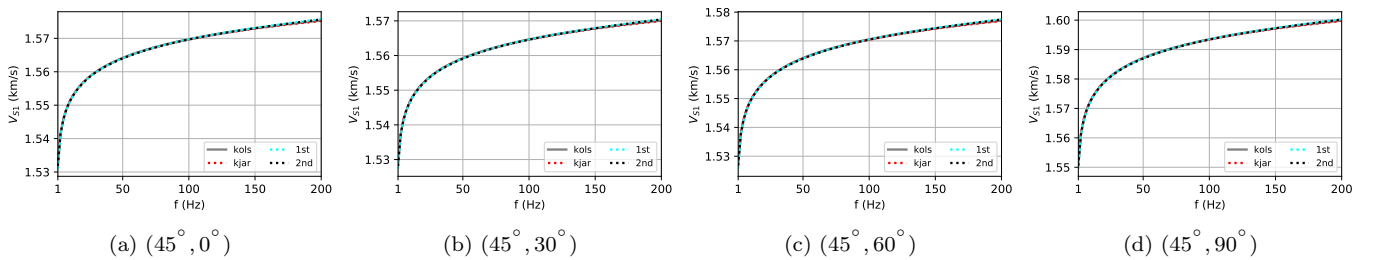


Figure 14: Similar to Figure 10 but for the  $S_1$  waves with  $\theta = 45^\circ$ .

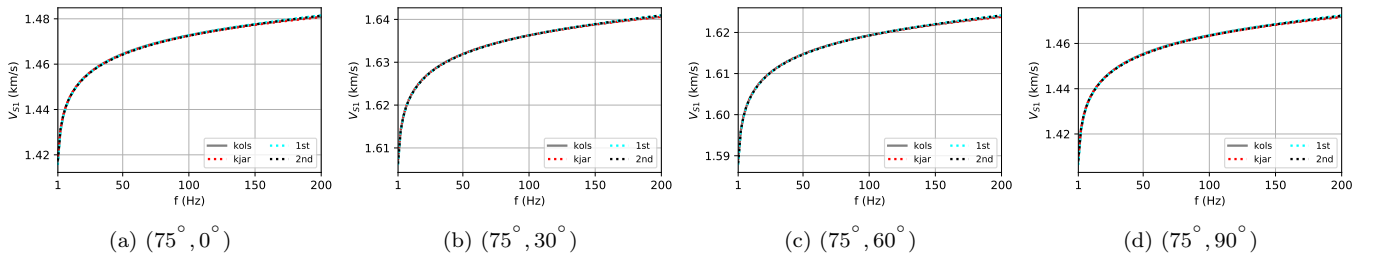


Figure 15: Similar to Figure 10 but for the  $S_1$  waves with  $\theta = 75^\circ$ .

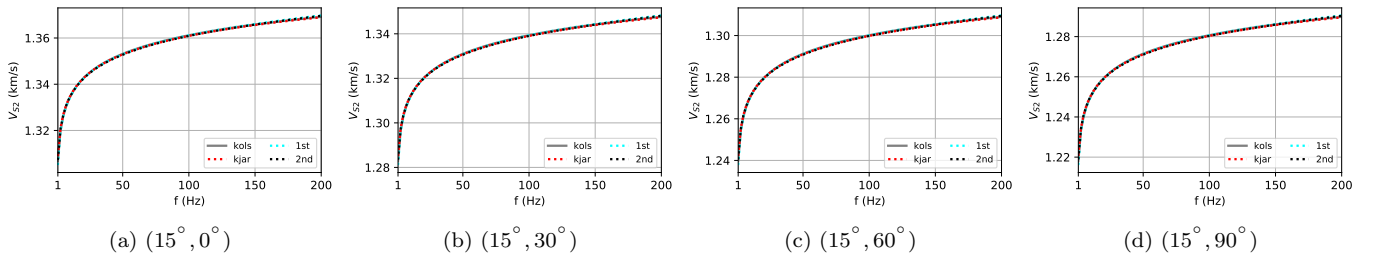


Figure 16: Similar to Figure 10 but for the  $S_2$  waves with  $\theta = 15^\circ$ .

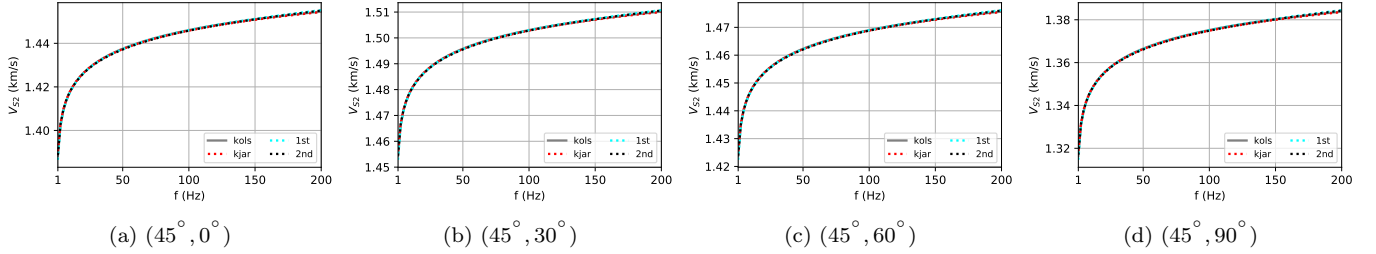


Figure 17: Similar to Figure 10 but for the  $S_2$  waves with  $\theta = 45^\circ$ .

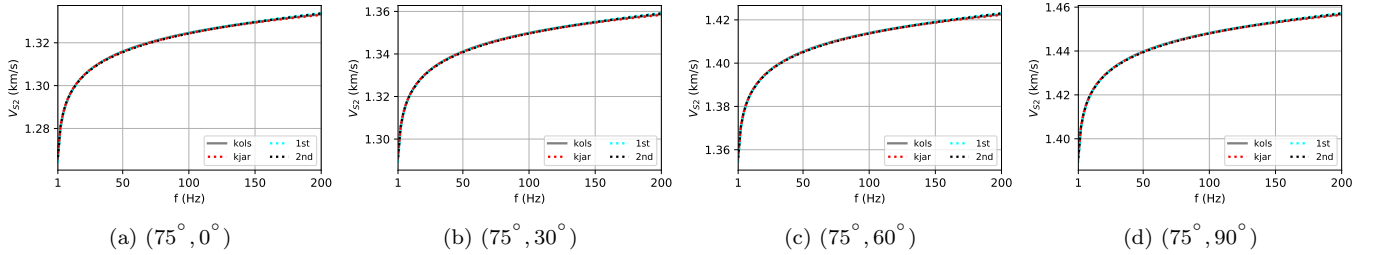


Figure 18: Similar to Figure 10 but for the  $S_2$  waves with  $\theta = 75^\circ$ .

#### 4.3. The variation of the Thomsen parameters with frequency

Figures 19 through 21 show the variation of the velocity-related Thomsen parameters with frequency. For any of these parameters, our nearly constant  $Q$  models are approximately identical to the Kolsky and Kjartansson models. All the velocity-related Thomsen parameters vary slightly with frequency. Figures 22 through 24 show the variation of the attenuation-related Thomsen parameters with frequency. The attenuation-related Thomsen parameters for the first- and second-order nearly constant  $Q$  models are accurate approximations to those for the Kolsky and Kjartansson models, respectively. For any of the attenuation-related Thomsen parameters, however, the difference between the first- and second-order nearly constant  $Q$  models (or the Kolsky and Kjartansson models) are clearly evident.

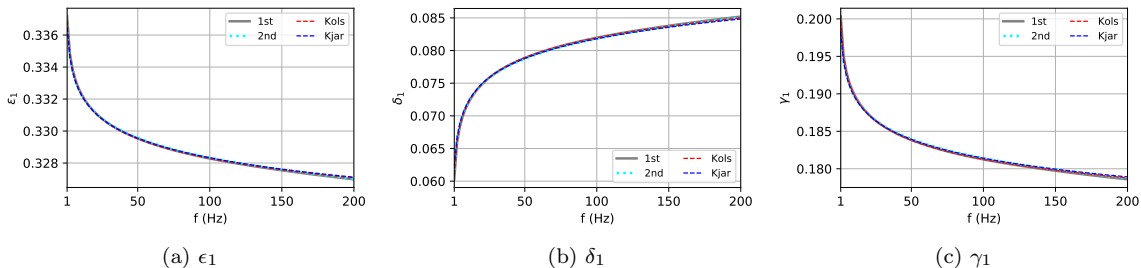


Figure 19: The variation of the Thomsen parameters  $\epsilon_1$ ,  $\delta_1$  and  $\gamma_1$  with frequency.

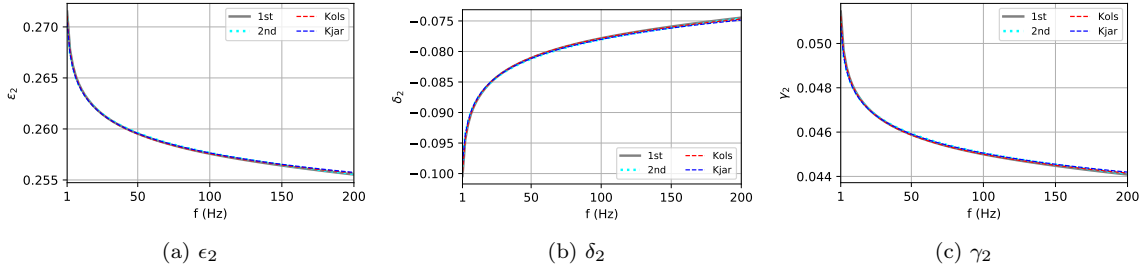


Figure 20: The variation of the Thomsen parameters  $\epsilon_2$ ,  $\delta_2$  and  $\gamma_2$  with frequency.

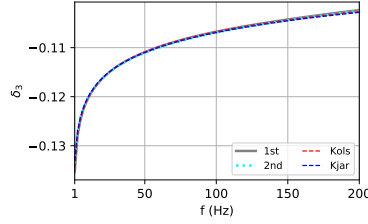


Figure 21: The Thomsen parameter  $\delta_3$  with frequency.

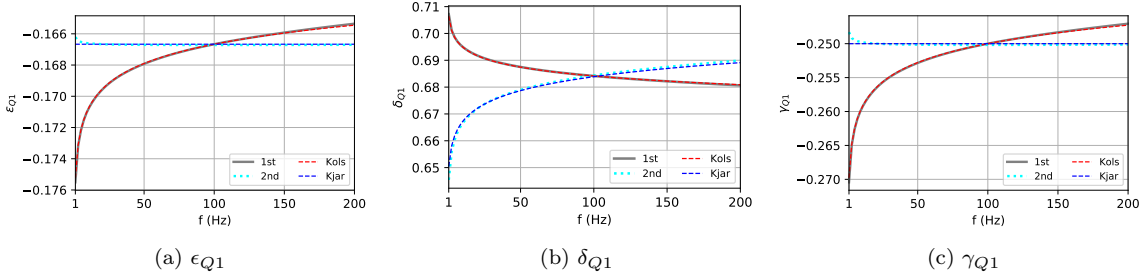


Figure 22: The variation of the Thomsen parameters  $\epsilon_{Q1}$ ,  $\delta_{Q1}$  and  $\gamma_{Q1}$  with frequency.

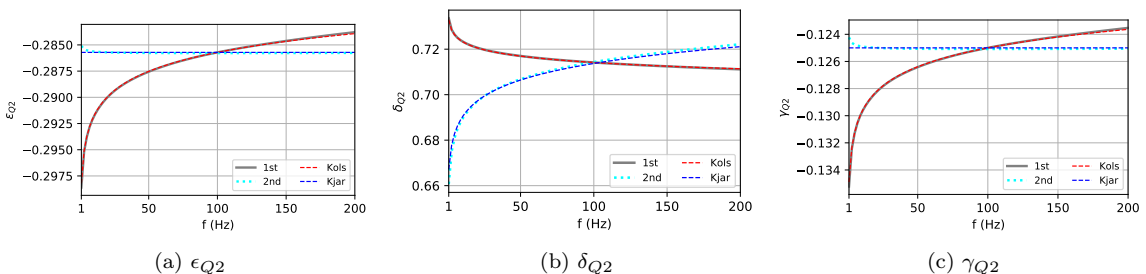


Figure 23: The variation of the Thomsen parameters  $\epsilon_{Q2}$ ,  $\delta_{Q2}$  and  $\gamma_{Q2}$  with frequency.

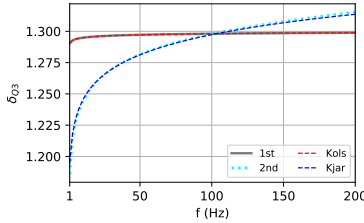


Figure 24: The variation of the Thomsen parameter  $\delta_{Q3}$  with frequency.

## 5. Nearly constant $Q$ wave equations for viscoelastic isotropy

As shown in equations 4.24 through 4.26 of HG2021, the viscoelastic anisotropic wave equations for the second-order nearly constant  $Q$  model are given by

$$\rho \frac{\partial^2 u_i}{\partial t^2} = \frac{\partial}{\partial x_j} \left( B_{ijkl}^{(0)} \frac{\partial u_k}{\partial x_l} \right) - \sum_{\ell=1}^L h_i^{(\ell)} + S_i, \quad (33)$$

$$\frac{\partial h_i^{(\ell)}}{\partial t} = s^{(\ell)} \left[ \frac{\partial}{\partial x_j} \left( B_{ijkl}^{(1)} \frac{\partial u_k}{\partial x_l} \right) - \sum_{\ell=1}^L \tilde{h}_i^{(\ell)} \right] - \frac{1}{\tau_{\sigma\ell}} h_i^{(\ell)}, \quad (34)$$

$$\frac{\partial \tilde{h}_i^{(\ell)}}{\partial t} = s^{(\ell)} \frac{\partial}{\partial x_j} \left( B_{ijkl}^{(2)} \frac{\partial u_k}{\partial x_l} \right) - \frac{1}{\tau_{\sigma}^{(\ell)}} \tilde{h}_i^{(\ell)}, \quad (35)$$

with

$$B_{ijkl}^{(0)} = M_{ijkl}^{(0)} + g M_{ijkl}^{(1)} + \frac{1}{2} g^2 M_{ijkl}^{(2)}, \quad (36)$$

$$B_{ijkl}^{(1)} = M_{ijkl}^{(1)} + g M_{ijkl}^{(2)}, \quad (37)$$

$$B_{ijkl}^{(2)} = \frac{1}{2} M_{ijkl}^{(2)}. \quad (38)$$

Here,  $h_i^{(\ell)}$  and  $\tilde{h}_i^{(\ell)}$  are memory variables. The indices are taken as  $i, j, k = 1, 2, 3$ , where 1, 2 and 3 correspond to  $x$ ,  $y$  and  $z$ , respectively. According to HG2021,  $s^{(\ell)}$  and  $g$  are given by

$$s^{(\ell)} = \frac{1}{\tau_{\sigma}^{(\ell)}} \left( \frac{\tau_{\epsilon}^{(\ell)}}{\tau_{\sigma}^{(\ell)}} - 1 \right), \quad (39)$$

$$g = \sum_{\ell=1}^L \frac{\frac{\tau_{\epsilon}^{(\ell)}}{\tau_{\sigma}^{(\ell)}} - 1}{1 + \omega_0^2 \left( \tau_{\sigma}^{(\ell)} \right)^2}, \quad (40)$$

where  $\tau_{\sigma}^{(\ell)}$  and  $\tau_{\epsilon}^{(\ell)}$  are the relaxation times in the  $\ell$ -th standard-linear-solid element of the weighting function.

Referring to equation 3.22 of HG2021, the matrix form of  $M_{ijkl}^{(n)}$ ,  $n = 0, 1, 2$ , is given by

$$\mathbf{M}^{(n)} = \begin{pmatrix} \frac{M_P^{(0)}}{Q_P^n} & \frac{M_P^{(0)}}{Q_P^n} - 2\frac{M_S^{(0)}}{Q_S^n} & \frac{M_P^{(0)}}{Q_P^n} - 2\frac{M_S^{(0)}}{Q_S^n} & 0 & 0 & 0 \\ \frac{M_P^{(0)}}{Q_P^n} - 2\frac{M_S^{(0)}}{Q_S^n} & \frac{M_P^{(0)}}{Q_P^n} & \frac{M_P^{(0)}}{Q_P^n} - 2\frac{M_S^{(0)}}{Q_S^n} & 0 & 0 & 0 \\ \frac{M_P^{(0)}}{Q_P^n} - 2\frac{M_S^{(0)}}{Q_S^n} & \frac{M_P^{(0)}}{Q_P^n} - 2\frac{M_S^{(0)}}{Q_S^n} & \frac{M_P^{(0)}}{Q_P^n} & 0 & 0 & 0 \\ 0 & 0 & 0 & \frac{M_S^{(0)}}{Q_S^n} & 0 & 0 \\ 0 & 0 & 0 & 0 & \frac{M_S^{(0)}}{Q_S^n} & 0 \\ 0 & 0 & 0 & 0 & 0 & \frac{M_S^{(0)}}{Q_S^n} \end{pmatrix}, \quad (41)$$

where  $M_P^{(0)}$  and  $M_S^{(0)}$  denote the reference bulk and shear moduli, respectively. Quantities  $Q_P$  and  $Q_S$  denote the reference quality factors of homogeneous plane P and S waves, respectively.

Since  $\mathbf{M}^{(n)}$  shares the same symmetry property as the stiffness matrix for an isotropic medium, the fourth-rank tensor form of equation 41 is written as

$$M_{ijkl}^{(n)} = \left( \frac{M_P}{Q_P^n} - 2\frac{M_S}{Q_S^n} \right) \delta_{ij} \delta_{kl} + \frac{M_S}{Q_S^n} \delta_{ik} \delta_{jl} + \frac{M_S}{Q_S^n} \delta_{il} \delta_{jk}, \quad (42)$$

where  $\delta_{ij}$  denotes the Kronecker delta.

Taking account of the Einstein summation convention, we derive

$$M_{ijkl}^{(n)} \frac{\partial u_k}{\partial x_l} = \left( \frac{M_P}{Q_P^n} - 2\frac{M_S}{Q_S^n} \right) \delta_{ij} \frac{\partial u_k}{\partial x_k} + \frac{M_S}{Q_S^n} \frac{\partial u_i}{\partial x_j} + \frac{M_S}{Q_S^n} \frac{\partial u_j}{\partial x_i}. \quad (43)$$

Assuming  $M_{ijkl}^{(n)}$  to be independent of the spatial coordinates, we derive

$$\frac{\partial}{\partial x_j} \left( M_{ijkl}^{(n)} \frac{\partial u_k}{\partial x_l} \right) = \frac{M_P}{Q_P^n} \frac{\partial}{\partial x_i} \left( \frac{\partial u_j}{\partial x_j} \right) + \frac{M_S}{Q_S^n} \frac{\partial^2 u_i}{\partial x_j \partial x_j} - \frac{M_S}{Q_S^n} \frac{\partial}{\partial x_i} \left( \frac{\partial u_j}{\partial x_j} \right). \quad (44)$$

The above equation can be rewritten in vector form as

$$\left\{ \frac{\partial}{\partial x_j} \left( M_{ijkl}^{(n)} \frac{\partial u_k}{\partial x_l} \right) \right\} = \frac{M_P}{Q_P^n} \nabla (\nabla \cdot \mathbf{u}) + \frac{M_S}{Q_S^n} \nabla^2 \mathbf{u} - \frac{M_S}{Q_S^n} \nabla (\nabla \cdot \mathbf{u}), \quad (45)$$

where symbol  $\{.\}$  denotes a three-element vector. Symbols  $\nabla$  and  $\nabla^2$  denote the gradient and Laplacian operators, respectively. Vector  $\mathbf{u} = (u_1, u_2, u_3)^T$  denotes the particle displacement vector, where indices “1”, “2” and “3” correspond to the  $x$ ,  $y$  and  $z$ , respectively.

The Laplacian operator can be rewritten as

$$\nabla^2 \mathbf{u} = \nabla (\nabla \cdot \mathbf{u}) - \nabla \times \nabla \times \mathbf{u}. \quad (46)$$

Hence, equation 45 can be written as

$$\left\{ \frac{\partial}{\partial x_j} \left( M_{ijkl}^{(n)} \frac{\partial u_k}{\partial x_l} \right) \right\} = \frac{M_P}{Q_P^n} \nabla (\nabla \cdot \mathbf{u}) - \frac{M_S}{Q_S^n} \nabla \times \nabla \times \mathbf{u}. \quad (47)$$

The bulk and shear moduli are expressed as

$$M_P = \rho v_P^2, \quad M_S = \rho v_S^2, \quad (48)$$

where  $v_P$  and  $v_S$  denote the velocities of P and S waves, which are defined at the reference frequency.

Substituting all the above results in this section into equations 33 through 38, the viscoelastic isotropic wave equations for the second-order nearly constant  $Q$  model are given in vector form by

$$\frac{\partial^2 \mathbf{u}}{\partial t^2} = b_P^{(0)} \nabla(\nabla \cdot \mathbf{u}) - b_S^{(0)} \nabla \times \nabla \times \mathbf{u} - \sum_{\ell=1}^L \mathbf{d}^{(\ell)} + \mathbf{f}, \quad (49)$$

$$\frac{\partial \mathbf{d}^{(\ell)}}{\partial t} = s^{(\ell)} \left( b_P^{(1)} \nabla(\nabla \cdot \mathbf{u}) - b_S^{(1)} \nabla \times \nabla \times \mathbf{u} - \sum_{\ell=1}^L \tilde{\mathbf{d}}^{(\ell)} \right) - \frac{1}{\tau_\sigma^{(\ell)}} \mathbf{d}^{(\ell)}, \quad (50)$$

$$\frac{\partial \tilde{\mathbf{d}}^{(\ell)}}{\partial t} = s^{(\ell)} \left( b_P^{(2)} \nabla(\nabla \cdot \mathbf{u}) - b_S^{(2)} \nabla \times \nabla \times \mathbf{u} \right) - \frac{1}{\tau_\sigma^{(\ell)}} \tilde{\mathbf{d}}^{(\ell)}, \quad (51)$$

where we have assumed the medium to be homogeneous. Vector  $\mathbf{f} = \mathbf{S}/\rho$  denotes the body force per unit mass, where  $\mathbf{S}$  denotes a vector of components  $S_i$ . Quantities  $\mathbf{d}^{(\ell)} = (d_x^{(\ell)}, d_y^{(\ell)}, d_z^{(\ell)})^T$  and  $\tilde{\mathbf{d}}^{(\ell)} = (\tilde{d}_x^{(\ell)}, \tilde{d}_y^{(\ell)}, \tilde{d}_z^{(\ell)})^T$  are the density-normalized memory variables in vector form. They are linked to the memory variables in the anisotropic wave equations 33 through 35 by the relations  $d_i^{(\ell)} = h_i^{(\ell)}/\rho$  and  $\tilde{d}_i^{(\ell)} = \tilde{h}_i^{(\ell)}/\rho$ . Quantities  $b_I^{(0)}$ ,  $b_I^{(1)}$  and  $b_I^{(2)}$ ,  $I = P$  and  $S$ , are given by

$$b_I^{(0)} = v_I^2 \left( 1 + \frac{g}{Q_I} + \frac{g^2}{2Q_I^2} \right), \quad (52)$$

$$b_I^{(1)} = \frac{v_I^2}{Q_I} \left( 1 + \frac{g}{Q_I} \right), \quad (53)$$

$$b_I^{(2)} = \frac{v_I^2}{2Q_I^2}. \quad (54)$$

Omitting all the terms associated with  $Q_I^2$ , the wave equations for the second-order nearly constant  $Q$  model reduce to the wave equations for the first-order model

$$\frac{\partial^2 \mathbf{u}}{\partial t^2} = a_P^{(0)} \nabla(\nabla \cdot \mathbf{u}) - a_S^{(0)} \nabla \times \nabla \times \mathbf{u} - \sum_{\ell=1}^L \mathbf{c}^{(\ell)} + \mathbf{f}, \quad (55)$$

$$\frac{\partial \mathbf{c}^{(\ell)}}{\partial t} = s^{(\ell)} \left( a_P^{(1)} \nabla(\nabla \cdot \mathbf{u}) - a_S^{(1)} \nabla \times \nabla \times \mathbf{u} \right) - \frac{1}{\tau_\sigma^{(\ell)}} \mathbf{c}^{(\ell)}, \quad (56)$$

(57)

with

$$a_I^{(0)} = v_I^2 \left( 1 + \frac{g}{Q_I} \right), \quad (58)$$

$$a_I^{(1)} = \frac{v_I^2}{Q_I}. \quad (59)$$

Here,  $\mathbf{c}^{(\ell)} = (c_x^{(\ell)}, c_y^{(\ell)}, c_z^{(\ell)})^T$  is a vector of the density-normalized memory variables.

## 6. Numerical wave modeling

Following HG2021, Figure 25 shows the P-wave parameters for the viscoelastic isotropic version of the Marmousi model. Using the P-wave model parameters as illustrated in Figure 25, we set the S-wave model parameters as

$v_S = v_P/2$  and  $Q_S = 7Q_P/10$ . All the model parameters are defined at the reference frequency  $f_0 = 40$  Hz. The  $z$ -component of the source function  $\mathbf{f}$  in equations 49 and 55 is initiated at  $x = 1.645$  km and  $z = 0.925$  km by a 40 Hz Ricker wavelet (Figure 26). The maximum frequency of the Ricker wavelet is less than 130 Hz.

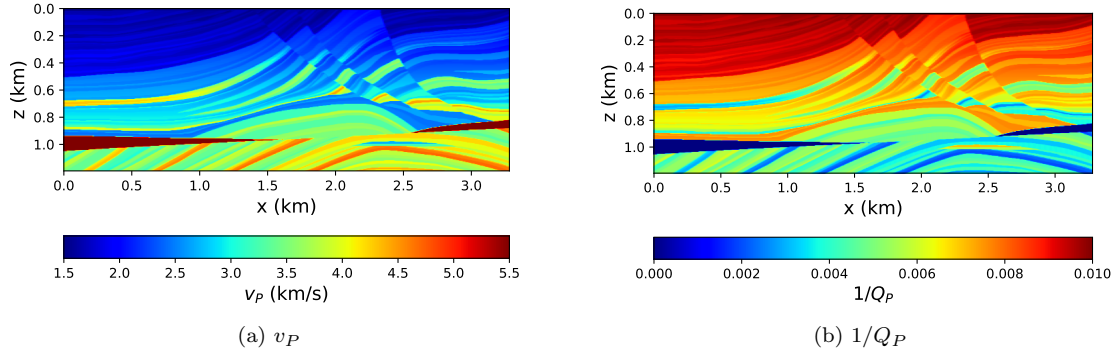


Figure 25: The P-wave model parameters in the viscoelastic Marmousi model.

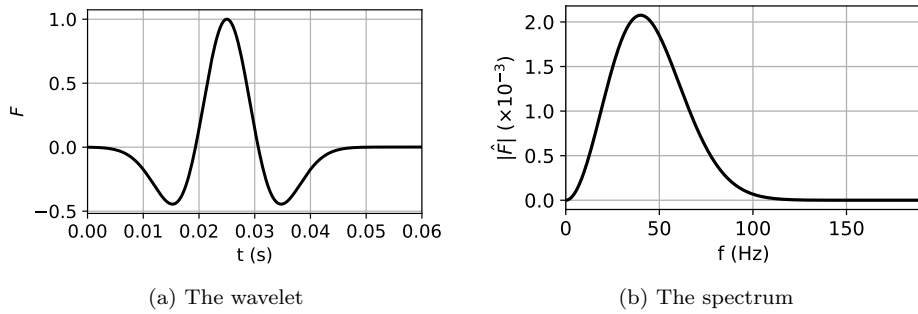


Figure 26: A 40 Hz Ricker wavelet and its amplitude spectrum.

The viscoelastic isotropic wave equations for the first- and second-order nearly constant  $Q$  models require the relaxation times of the weighting function in a frequency range of interest. Referring to HG2021, Table 2 shows the relaxation times of the weighting function in the frequency range [1, 200] Hz, which is not ideally matched to the effective frequency range of the Ricker wavelet. Referring to [6], we take into account the scaling property of the weighting function:

$$\tau_{el}^{(a)} = \frac{\tau_{el}^{(b)}}{\xi}, \quad \tau_{\sigma l}^{(a)} = \frac{\tau_{\sigma l}^{(b)}}{\xi}, \quad (60)$$

where  $\xi$  denotes a scale factor. Quantities  $\tau_{el}^{(b)}$  and  $\tau_{\sigma l}^{(b)}$  denote the relaxation times of the weighting function in the frequency range  $[\omega_L, \omega_U]$ . Quantities  $\tau_{el}^{(a)}$  and  $\tau_{\sigma l}^{(a)}$  denote the relaxation times for the frequency range  $[\xi\omega_L, \xi\omega_U]$  after scaling. Dividing the relaxation times in Table 2 by 0.65, we obtain the relaxation times of the weighting function in the frequency range [0.65, 130] Hz, as illustrated in Table 3. To verify the validity of the weighting function, we use the relaxation times in Table 3 to compute the quality factor and phase velocity of a homogeneous plane wave in the viscoacoustic case. Figure 27 shows that after scaling the valid frequency range of interest the quality factors and phase velocities for the first- and second-order nearly constant  $Q$  models fit well with those for the Kolsky and Kjartansson models, respectively. Figure 28 indicates that the phase velocities for all these models are quite close to each other. These results for the quality factor and phase velocity are consistent with the results for orthorhombic anisotropy (Figures 1 through Figure 9).

Table 2: Optimal relaxation times for the five-element weighting function in the frequency range [1, 200] Hz, from Table 11 of [6].

| $\ell$ | $\tau_\sigma^{(\ell)}$ (s) | $\Delta\tau^{(\ell)} = \tau_\epsilon^{(\ell)} - \tau_\sigma^{(\ell)}$ (s) |
|--------|----------------------------|---|
| 1      | $1.8230838 \times 10^{-1}$ | $2.7518001 \times 10^{-1}$  |
| 2      | $3.2947348 \times 10^{-2}$ | $3.0329269 \times 10^{-2}$  |
| 3      | $8.4325390 \times 10^{-3}$ | $6.9820198 \times 10^{-3}$  |
| 4      | $2.3560480 \times 10^{-3}$ | $1.9223614 \times 10^{-3}$  |
| 5      | $5.1033826 \times 10^{-4}$ | $7.2390630 \times 10^{-4}$  |

Table 3: Optimal relaxation times for the five-element weighting function in the frequency range [0.65, 130] Hz. Referring to equations 60, the relaxation times for this frequency range are obtained by dividing the relaxation times in Table 2 by 0.65.

| $\ell$ | $\tau_\sigma^{(\ell)}$ (s) | $\Delta\tau^{(\ell)} = \tau_\epsilon^{(\ell)} - \tau_\sigma^{(\ell)}$ (s) |
|--------|----------------------------|---|
| 1      | $2.8047443 \times 10^{-1}$ | $4.2335386 \times 10^{-1}$  |
| 2      | $5.0688228 \times 10^{-2}$ | $4.6660414 \times 10^{-2}$  |
| 3      | $1.2973137 \times 10^{-2}$ | $1.0741569 \times 10^{-2}$  |
| 4      | $3.6246892 \times 10^{-3}$ | $2.9574791 \times 10^{-3}$  |
| 5      | $7.8513578 \times 10^{-4}$ | $1.1137020 \times 10^{-3}$  |

We use the finite difference (FD) method [e.g., 7] to solve the viscoelastic isotropic wave equations for the first- and second-order nearly constant  $Q$  models (equations 55 and 56, and equations 49 through 51) in the [x, z] plane. The relaxation times in Table 3 are used in the viscoelastic isotropic wave equations. To analyze the effect of dissipation on wave propagation, we also model the elastic wave propagation in the Marmousi model with  $Q_P = Q_S = \infty$ . The Marmousi model is discretized by a spatial grid interval  $\Delta x = \Delta z = 5$  m. The time step in the finite difference method is  $10^{-4}$  s. The first temporal derivative ( $\partial/\partial t$ ) is approximated by the second-order FD operator. The second temporal derivative ( $\partial^2/\partial t^2$ ) is approximated by applying the second-order FD operator twice. The first spatial derivatives ( $\partial/\partial x$  and  $\partial/\partial z$ ) are approximated by the fourteenth-order FD operator. The second spatial derivatives ( $\partial^2/\partial x^2$  and  $\partial^2/\partial z^2$  and  $\partial^2/\partial x\partial z$ ) are approximated by applying the fourteenth-order FD operator twice. The FD stencil weights can be found in [8]. The Marmousi model is surrounded by a perfectly matched layer [9] of 40 grid points to absorb the artificial reflections from the model boundaries. The receivers are located at the surface of the model.

A comparison between Figures 29, 30 and 31 shows that the shot-gather seismograms for the elastic medium includes more high-frequency components than the viscoelastic shot-gather seismograms. Figures 32 through 37, which give individual seismograms at specific receiver distances, show that (1) the amplitudes of the viscoelastic waveforms are decayed significantly; (2) the waveforms for the first-order nearly constant  $Q$  wave equations is slightly different from those for the second-order nearly constant  $Q$  wave equations. Since the first- and second-order nearly constant  $Q$  models provide approximately identical velocities (28), the quality factor difference between these two models is the major cause of their waveform difference.

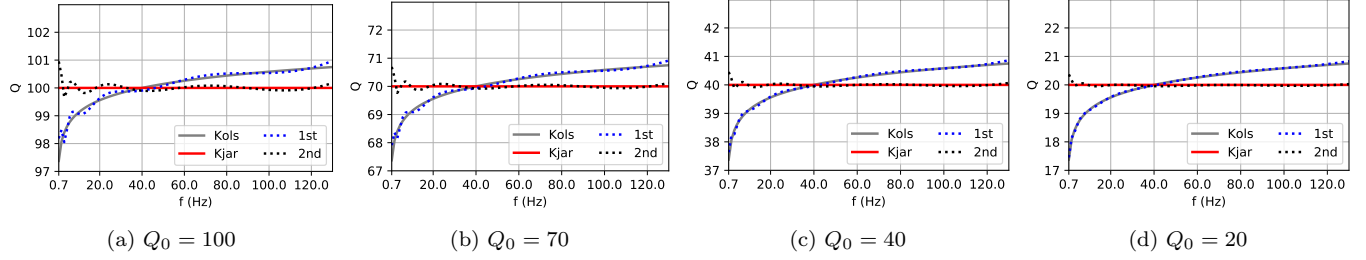


Figure 27: The variation of the quality factor with frequency in the weak-, moderate- and strong-attenuation cases. The quantity  $Q_0$  denotes the quality factor at the reference frequency. The legend abbreviations “Kols”, “Kjar”, “1st” and “2nd” denote the Kolsky and Kjartansson models, and the first- and second-order nearly constant  $Q$  models, respectively. The relaxation times for the first- and second-order nearly constant  $Q$  models are initiated by the values in Table 3. The reference frequency is 40 Hz.

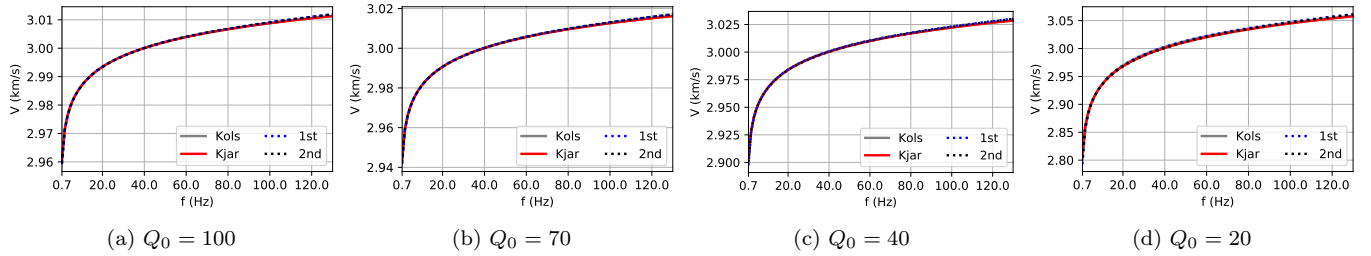


Figure 28: Similar to Figure 27 but for the phase velocity. The reference velocity is 3 km/s.

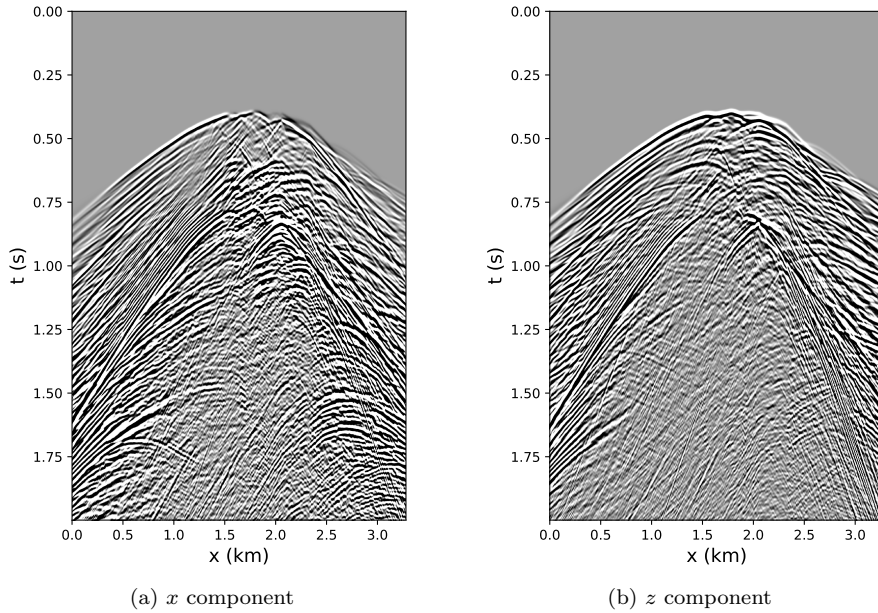


Figure 29: The shot-gather seismograms of the particle displacement from the elastic isotropic wave equations. Both plots are illustrated in the same color scale, which is bounded by the minimum and maximum of the  $x$  and  $z$  components of the particle displacement. A gain function  $t^{0.8}$  is applied to the seismograms.

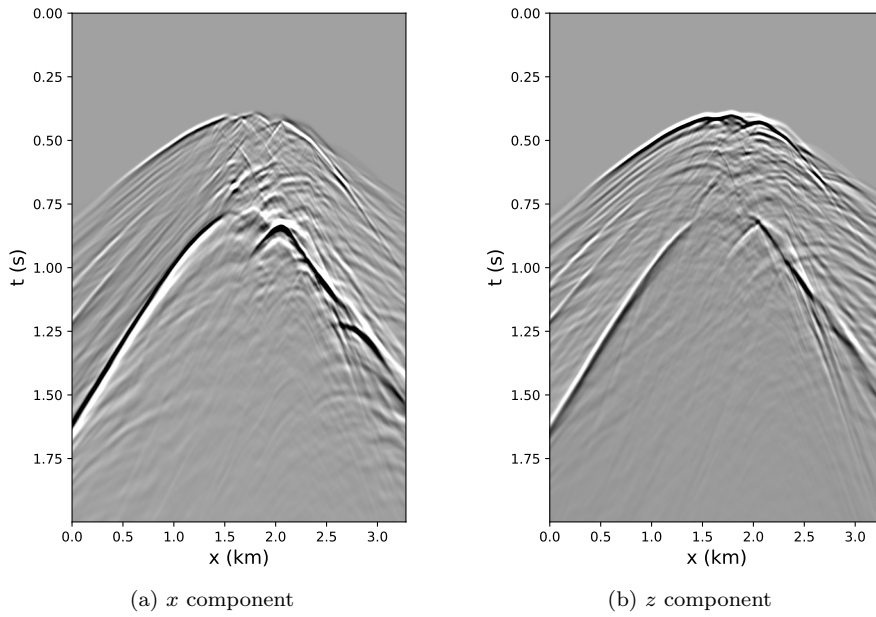


Figure 30: Similar to Figure 29 but from the viscoelastic isotropic wave equations for the first-order nearly constant  $Q$  model. The color scale in the plots is the same as those in Figure 29.

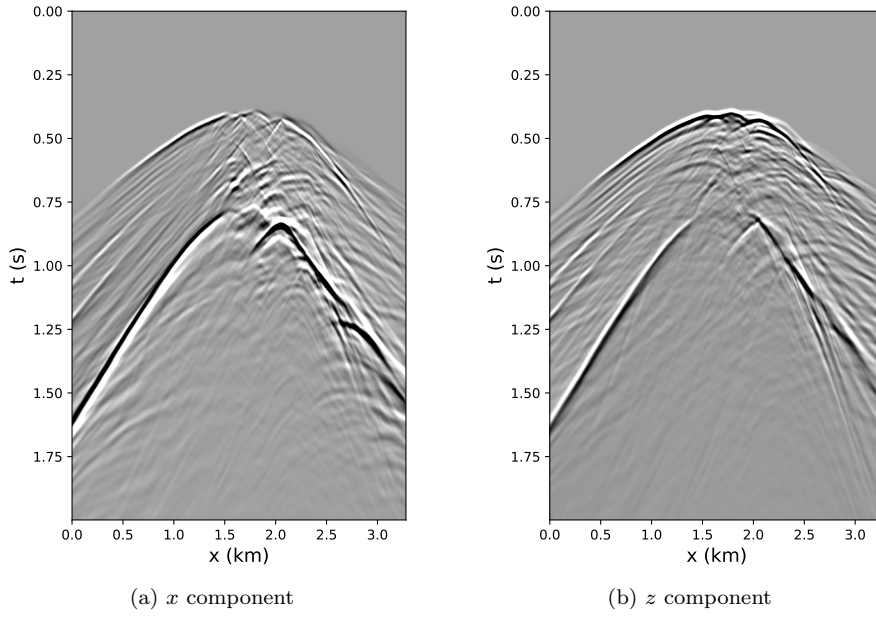


Figure 31: Similar to Figure 29 but from the viscoelastic isotropic wave equations for the second-order nearly constant  $Q$  model. The color scale in the plots is the same as those in Figure 29.

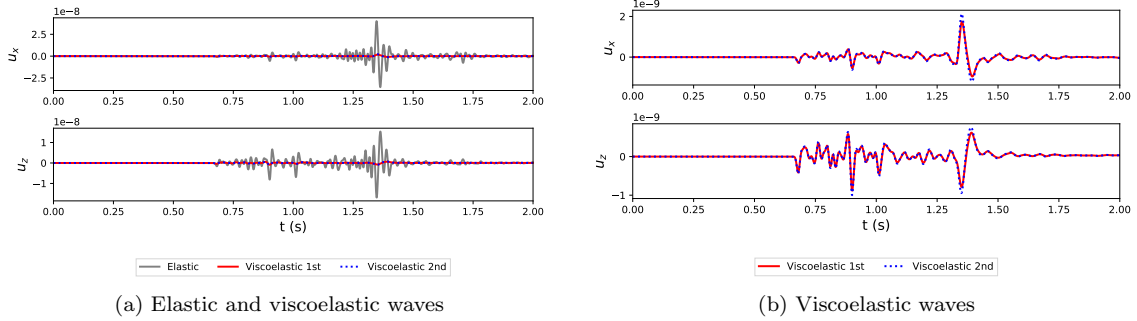


Figure 32: Single-trace seismograms for the receiver at  $x_R = 0.4$  km. The legend abbreviations “Elastic”, “Viscoelastic 1st” and “Viscoelastic 2nd” correspond to the elastic wave equations ( $Q_P = Q_S = \infty$ ) and the first- and second-order nearly constant  $Q$  wave equations, respectively. Plots (a) and (b) show the same viscoelastic waveforms at different scales.

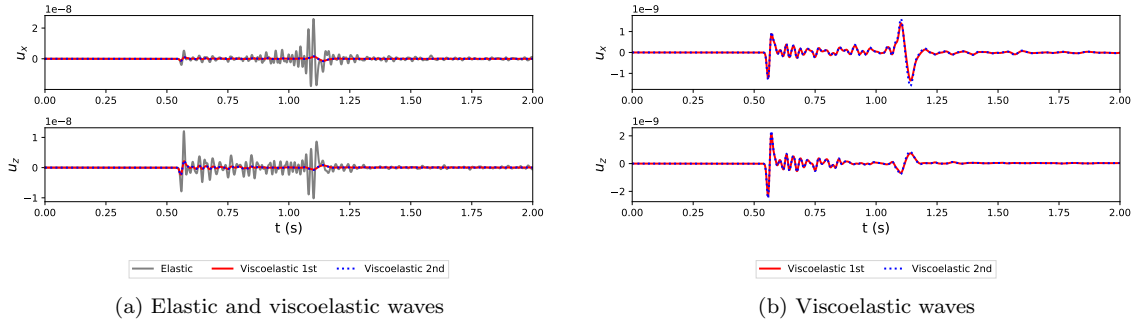


Figure 33: Similar to Figure 32 but for the receiver at  $x_R = 0.8$  km.

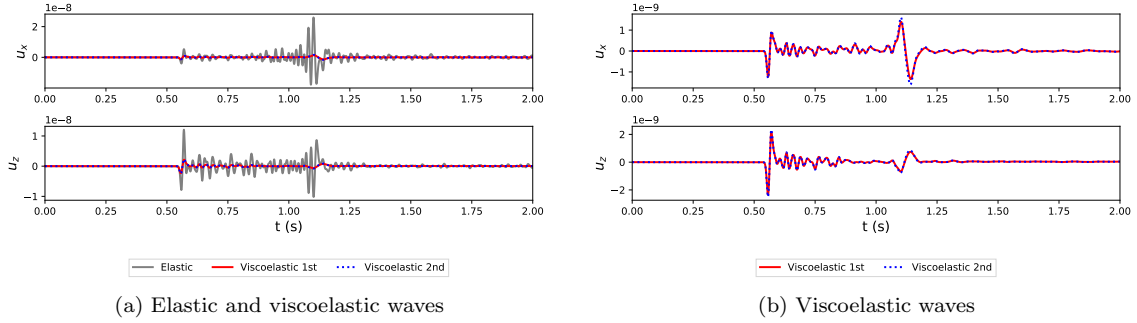


Figure 34: Similar to Figure 32 but for the receiver at  $x_R = 1.2$  km.

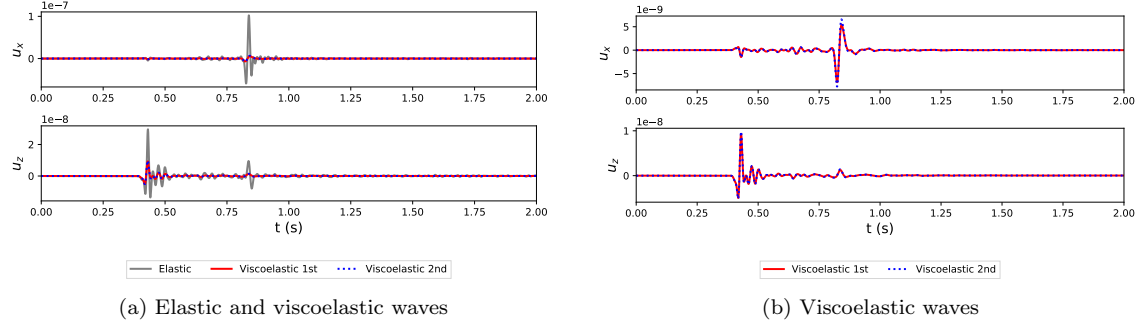


Figure 35: Similar to Figure 32 but for the receiver at  $x_R = 2.08$  km.

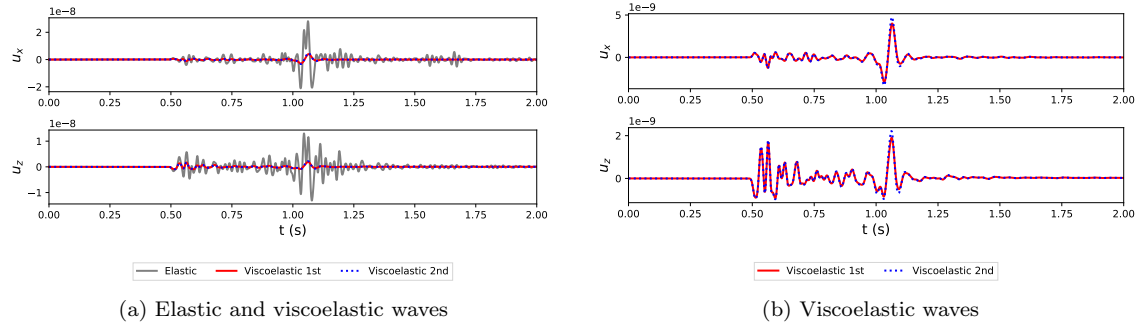


Figure 36: Similar to Figure 32 but for the receiver at  $x_R = 2.48$  km.

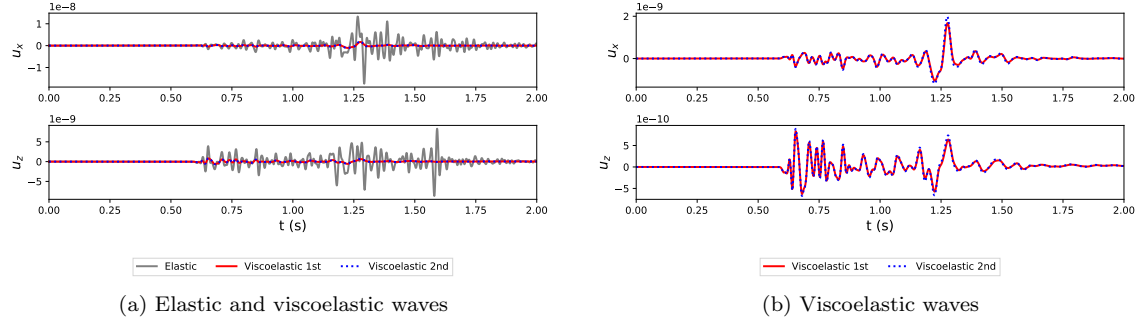


Figure 37: Similar to Figure 32 but for the receiver at  $x_R = 2.88$  km.

## References

- [1] V. Cerveny, *Seismic ray theory*, Cambridge University Press, 2001.
- [2] J. M. Carcione, Constitutive model and wave equations for linear, viscoelastic, anisotropic media, *Geophysics* 60 (2) (1995) 537–548.
- [3] L. Knopoff, *Q*, *Reviews of Geophysics* 2 (4) (1964) 625–660.

- [4] I. Tsvankin, Anisotropic parameters and P-wave velocity for orthorhombic media, *Geophysics* 62 (4) (1997) 1292–1309.
- [5] Y. Zhu, I. Tsvankin, Plane-wave attenuation anisotropy in orthorhombic media, *Geophysics* 72 (1) (2007) D9–D19.
- [6] Q. Hao, S. Greenhalgh, Nearly constant  $Q$  models of the generalized standard linear solid type and the corresponding wave equations, *Geophysics* 86 (4) (2021) in press.
- [7] H. Emmerich, M. Korn, Incorporation of attenuation into time-domain computations of seismic wave fields, *Geophysics* 52 (9) (1987) 1252–1264.
- [8] C. Chu, P. L. Stoffa, Application of normalized pseudo-laplacian to elastic wave modeling on staggered grids, *Geophysics* 76 (5) (2011) T13–T21.
- [9] F. H. Drossaert, A. Giannopoulos, A nonsplit complex frequency-shifted PML based on recursive integration for FDTD modeling of elastic waves, *Geophysics* 72 (2) (2007) T9–T17.